Nanoscale

PAPER

View Article Online
View Journal | View Issue

Cite this: *Nanoscale*, 2023, **15**, 14584

High-efficiency visible-light-driven oxidation of primary C–H bonds in toluene over a $CsPbBr_3$ perovskite supported by hierarchical TiO_2 nanoflakes†

Jiayu Yi,[a] Sunzai Ke,[a] Suwei Lu,[a] Bo Weng,[b] Lijuan Shen,[a] Xuhui Yang,[a] Hun Xue,[a] Min-Quan Yang *[a] and Qingrong Qian *[a]

Photocatalytic oxidation of toluene to valuable fine chemicals is of great significance, yet faces challenges in the development of advanced catalysts with both high activity and selectivity for the activation of inert C(sp^3)–H bonds. Halide perovskites with remarkable optoelectronic properties have shown to be prospective photoactive materials, but the bulky structure with a small surface area and severe recombination of photogenerated electron–hole pairs are obstacles to application. Here, we fabricate a hierarchical nanoflower-shaped $CsPbBr_3/TiO_2$ heterojunction by assembling $CsPbBr_3$ nanoparticles on 2D TiO_2 nanoflake subunits. The design significantly downsizes the size of $CsPbBr_3$ from micrometers to nanometers, and forms a type II heterojunction with intimate interfacial contact between $CsPbBr_3$ and TiO_2 nanoflakes, thereby accelerating the separation and transfer of photogenerated charges. Moreover, the formed hierarchical heterojunction increaseslight absorption by refraction and scattering, offers a large surface area and enhances the adsorption of toluene molecules. Consequently, the optimized $CsPbBr_3/TiO_2$ exhibits a high performance (10 200 μmol g^{-1} h^{-1}) for photocatalytic toluene oxidation with high selectivity (85%) for benzaldehyde generation under visible light. The photoactivity is about 20 times higher than that of blank $CsPbBr_3$, and is among the best photocatalytic performances reported for selective oxidation of toluene under visible light irradiation.

Received 6th July 2023,
Accepted 4th August 2023

DOI: 10.1039/d3nr03282e

rsc.li/nanoscale

Introduction

The direct oxidation of toluene to high-added-value fine chemicals, such as alcohols and aldehydes, is one of the most important conversions in the chemical industry.[1–4] However, due to the inertness and high bond dissociation energy (89.8 kcal mol^{-1}) of the C(sp^3)–H bond,[5] the activation of toluene generally needs to be performed under harsh reaction conditions (high pressure and temperature) and with the assistance of specific metal complexes or aggressive oxidants, which is expensive, energy intensive and causes negative impacts on the environment.[6–8] Solar-driven photocatalytic aerobic oxidation using molecular O_2 as an oxidant represents a promising methodology to overcome these challenges, but the overall photocatalytic performance reported so far is still unsatisfactory due to the lack of desired photocatalysts with broad optical absorption windows, efficient charge separation, and high product selectivity.[9–11]

Over the past years, halide perovskite materials have triggered wide attention in photocatalysis because of their outstanding optical and electronic properties.[12–16] High charge carrier mobility, visible light absorption, and tunable band structures enable them to be potential competitors for photocatalytic oxidation of toluene.[17,18] Nevertheless, single-component halide perovskites typically evolve into bulky aggregates with a large particle size (several to tens of micrometers), which leads to severe bulk recombination of charge carriers and restricts the photoactivity.[19,20] To tackle this problem, the construction of a heterojunction is an effective strategy. Hybridization of the halide perovskite with preferred substrates not only can prevent the aggregation of the halide perovskite to mediate the bulk recombination of photoexcited electron–hole pairs, but also can establish an interfacial built-in electric field to further facilitate the spatial charge transfer and separation.[21]

Moreover, the catalytic functions of photocatalysts also strongly depend on the nanostructure.[22,23] To realize high

[a]*College of Environmental and Resource Sciences, College of Carbon Neutral Modern Industry, Fujian Key Laboratory of Pollution Control & Resource Reuse, Fujian Normal University, Fuzhou 350117, P.R. China. E-mail: yangmq@fjnu.edu, cnqrqian@fjnu.edu.cn*

[b]*cMACS, Department of Microbial and Molecular Systems, KU Leuven, Celestijnenlaan 200F, 3001 Leuven, Belgium*

† Electronic supplementary information (ESI) available. See DOI: https://doi.org/10.1039/d3nr03282e

photocatalytic performance, the delicate design of a well-defined nanostructure for heterojunction composites is also critical.[24–27] For diverse structural configurations, 3D hierarchical flower-like nanostructures constructed using 2D nanoflake subunits have demonstrated intrinsic advantages for photocatalysis. Such hierarchical structures can strengthen the light absorption of photocatalysts by multi-light reflection and scattering within the nanoflake subunits, and prohibit the aggregation of 2D nanoflakes to afford a large surface area with abundant active sites.[28,29] In addition, the nanoflake subunits will greatly shorten the diffusion path of charges, thereby facilitating the separation and transfer of photogenerated charges to the surface for redox reactions.[30,31] Thus, the development of advanced 2D subunit-assembled hierarchical structures with a heterogeneous junction would be promising for high-efficiency photocatalytic toluene oxidation.

Here, inspired by the above considerations, we design and fabricate a hierarchical nanoflower-shaped $CsPbBr_3/TiO_2$ (abbreviated as CPB/TiO_2) heterojunction composed of TiO_2 nanoflake-supported all-inorganic $CsPbBr_3$ perovskite nanoparticles. Benefiting from the composition and nanostructure engineering, the CPB/TiO_2 heterojunction displays excellent performance for photocatalytic toluene oxidation under the irradiation of visible light. The optimized 20%CPB/TiO_2 heterojunction composite delivers a toluene conversion rate of 10 200 μmol g^{-1} h^{-1} and a high selectivity of 85% towards benzaldehyde (benzyl alcohol as the main by-product). This performance outperforms most of the state-of the-art catalysts in the literature for visible-light-driven oxidation of toluene. This work provides a new idea by constructing a hierarchical heterojunction structure over halide perovskite materials for high-efficiency photocatalytic toluene conversion.

Experimental section

Materials

Cesium bromide (CsBr, 99.999%), lead bromide ($PbBr_2$, 99.0%) and tetrahydrofuran (THF) were purchased from Macklin (Shanghai, China). *N*,*N*-Dimethylformamide (DMF), toluene, tetrabutyl titanate (TBOT), ethanol (EtOH), concentrated hydrochloric acid (HCl, 36%), acetic acid and glycerol were obtained from Sinopharm Chemical Reagent Co., Ltd (Shanghai, China). All chemicals and solvents were used without further purification.

Synthesis of mesoporous hierarchical TiO_2 nanoflowers

Typically, 1.5 g of Pluronic F127 was dispersed in a mixed solvent of 2.4 mL of acetic acid, 3.2 mL of concentrated hydrochloric acid (HCl) and 30 mL of tetrahydrofuran (THF). After vigorously stirring for 20 min, 3.4 mL of tetrabutyl titanate (TBOT) and 0.2 mL of H_2O were added subsequently to obtain a clear primrose yellow solution. After that, the solution was dried in an oven at 45 °C for 24 h to form a light-yellow gel. Then, 1.0 g of the gel was added into 25 mL of ethanol (EtOH) and 5 mL of glycerin under vigorous stirring. After 20 min, the transparent solution was transferred to a 50 mL Teflon-lined autoclave, heated at 150 °C for 15 h, and then cooled naturally to room temperature. The precipitate was washed with ethanol and dried in an oven at 60 °C.[32] Finally, the precipitate was calcined in a muffle furnace at 400 °C for 5 h at a heating rate of 1 °C min^{-1} to obtain the hierarchical TiO_2 nanoflowers. To synthesize the collapsed TiO_2 without the hierarchical nanoflower structure, the precipitate was calcined in the same muffle furnace at 400 °C for 5 h, but at a heating rate of 5 °C min^{-1}.

Synthesis of $CsPbBr_3/TiO_2$ composites and blank $CsPbBr_3$

$CsPbBr_3/TiO_2$ composites were synthesized according to an antisolvent precipitation method at room temperature.[33] Typically, 1 mmol CsBr and 1 mmol $PbBr_2$ were dissolved in 10 mL of *N*,*N*-dimethylformamide (DMF) by ultrasonication to form a precursor solution. Meanwhile, 100 mg of TiO_2 was dispersed in 10 mL of DMF and stirred to form a uniform white dispersion. Then a certain amount of the $CsPbBr_3$ precursor solution was added into the TiO_2 dispersion under ultrasonication. Then, the mixture was added dropwise into 50 ml of toluene and stirred vigorously for 30 min. After that, the solution was centrifuged at 8000 rpm for 3 min. The precipitate was collected and dried in a vacuum oven. A series of *x*% $CsPbBr_3/TiO_2$ composites were synthesized by changing the volume of the added $CsPbBr_3$ precursor solution, where *x* is the mass ratio of $CsPbBr_3$ in the composite (*x* = 10, 20, 30, and 40). Blank $CsPbBr_3$ was prepared by the same procedure without the addition of TiO_2.

Characterization

Scanning electron microscopy (SEM) images were captured using a Hitachi 8100. Transmission electron microscopy (TEM) and high-resolution transmission electron microscopy (HRTEM) images were recorded using a JEM-2100F EX microscope at an accelerating voltage of 200 kV. The Brunauer–Emmett–Teller (BET) specific surface area was measured using an N_2 adsorption–desorption instrument (BELSORP-mini II). The X-ray diffraction (XRD) patterns of the catalysts were characterized on a Bruker D8 Advance X-ray diffractometer operated at 40 kV and 40 mA with Cu Kα radiation and 2θ ranging from 10° to 80°. The UV-vis diffuse reflectance spectra (DRS) were obtained on a CARY-100 spectrophotometer (Agilent) using 100% $BaSO_4$ powder as a standard sample. X-ray photoelectron spectroscopy (XPS) spectra were recorded using an X-ray photoelectron spectrometer (Thermo Escalab 250 electron spectrometer) with Al-Kα radiation. Raman spectra were obtained using a laser at a wavelength of 785 nm (Thermo Fisher Scientific, DXR 2xi). Photoluminescence (PL) spectra of solid samples were obtained using an RF-5301PC spectrophotometer (Shimadzu, Japan) with a 435 nm excitation wavelength.

Electron paramagnetic resonance (EPR) measurements were performed at room temperature using a Magnettech ESR5000X spectrometer. In general, 10 mg samples were dispersed in a mixed solution of 2 mL of CH_3CN containing 1 mL

of toluene and 2 μL of 5,5-dimethyl-1-pyrroline-*N*-oxide (DMPO). The suspension was then transferred into a glass capillary. The sealed glass tube was then placed in the microwave cavity of an EPR spectrometer and exposed to a 300 W Xe lamp source (CEL-PF300-T8, Beijing China Education Au-light Co., Ltd) at room temperature.

Photoelectrochemical measurements

The photoelectrochemical analysis was carried out in a conventional three-electrode cell using a Pt plate and an Ag/AgCl electrode as the counter electrode and the reference electrode, respectively. The working electrode was prepared on fluorine-doped tin oxide (FTO) glass that was cleaned by ultrasonication in ethanol for 1 h. Typically, 5 mg of the catalyst was dispersed in 0.5 mL of isopropanol to obtain a slurry. After that, 20 μL of the slurry was dropped onto FTO with a size of 1 cm^2 and dried in air. The electrochemical impedance spectroscopy (EIS) measurement was performed in an electrolyte of tetrabutylammonium hexafluorophosphate ($TBAPF_6$) in ethyl acetate (EA). The transient photocurrent was tested in the same electrolyte and a 300 W xenon lamp (CEL-PF300-T8, Beijing China Education Au-light Co., Ltd) equipped with a 420 nm cutoff filter ($\lambda \geq 420$ nm) was used as the light source. Mott–Schottky measurement was performed in an electrolyte of 0.1 M $TBAPF_6$ in CH_2Cl_2.

Density functional theory (DFT) calculations

DFT calculations were carried out using the Vienna *ab initio* simulation package (VASP) with the projector-augmented-wave (PAW) method.[34] The Perdew–Burke–Ernzerhof (PBE) scheme was used for the exchange correlation function, employing the generalized gradient approximation (GGA).[35] The electronic wave function was expanded using a plane wave basis with an energy cutoff of 500 eV. The energy convergence criterion was set to 1.0×10^{-5} eV, and the force convergence criterion was set to 0.03 eV $Å^{-1}$ for each atom. For the $CsPbBr_3$ (110) and TiO_2 (101) slabs, a $6 \times 3 \times 1$ and $3 \times 9 \times 1$ *k*-point mesh was used, respectively. A 30 Å vacuum layer along the *z*-direction was used to prevent unintended periodic interactions between adjacent slabs. The $CsPbBr_3/TiO_2$ heterostructure model consists of two $CsPbBr_3$ layers and one TiO_2 layer, with a 20 Å vacuum space along the *z*-direction. To save computing resources, a $1 \times 1 \times 1$ *k*-point mesh was employed for the $CsPbBr_3/TiO_2$ heterostructure. The van der Waals interactions between TiO_2 and $CsPbBr_3$ were taken into account using the DFT-D3 correction method.

Photocatalytic activity measurements

All photocatalytic reactions were conducted in a quartz reactor. Typically, 10 mg of the photocatalyst and 1 mL of toluene (9.4 mmol) were dispersed in a reactor containing 2 mL of acetonitrile. The reactor was purged with O_2 for 10 min, and then irradiated with visible light ($\lambda > 420$ nm) using a 300 W xenon lamp (CEL-PF300-T8, Beijing China Education Au-light Co., Ltd). After light irradiation for 2 h, the liquid product was analyzed by gas chromatography (GC-2030, Shimadzu, Japan, FID detector, nitrogen (N_2) as the carrier gas) after centrifuging the suspension at 10 000 rpm for 3 min.

Results and discussion

Characterization of catalysts

The 3D hierarchical CPB/TiO_2 heterostructure was prepared by a simple anti-solvent precipitation method with the addition of TiO_2 nanoflowers into the precursor solution of $CsPbBr_3$, as schematically illustrated in Fig. 1a. X-ray diffraction (XRD) was exploited to characterize the crystal structure of blank $CsPbBr_3$, CPB/TiO_2 composites and TiO_2. As shown in Fig. 1b, the diffraction peaks at 15.1°, 21.5°, 30.7°, 34.4°, and 43.8° can be ascribed to the monoclinic $CsPbBr_3$ (100), (110), (200), (210) and (220) planes (JCPDS no. 18-0364).[36–38] In addition, the peaks at 25.3°, 37.7°, 48.0°, 53.8°, 55.0°, and 62.6° can be attributed to the (101), (004), (200), (105), (211), and (204) planes of anatase TiO_2, respectively.[32] The XRD patterns of CPB/TiO_2 composites indicate both characteristic peaks of $CsPbBr_3$ and TiO_2, and the peak intensity of $CsPbBr_3$ increases as the $CsPbBr_3$ content increases (Fig. S1†).

Raman spectra were used to further confirm the composition of the synthesized catalysts. As shown in Fig. 1c, the peaks at 151 cm^{-1} (E_g), 403 cm^{-1} (E_g), 523 cm^{-1} ($A_{1g} + B_{1g}$), and 646 cm^{-1} (E_g) belong to the anatase TiO_2 vibration modes. A new peak of 74 cm^{-1} assigned to the vibrational mode of the $[PbBr_6]^{4-}$ octahedron of $CsPbBr_3$ is observed in the CPB/TiO_2 composite.[39–41] The characteristic peak of $CsPbBr_3$ is also enhanced with the increment of the loading amount of $CsPbBr_3$ (Fig. S2†). This coincides with the XRD analysis, validating the successful preparation of the CPB/TiO_2 composites. Notably, after the growth of $CsPbBr_3$ on the TiO_2 nanosheets, the Raman peaks of TiO_2 shift to a lower wavenumber compared to that of blank TiO_2. The shift indicates an increase in the bond length and a decrease in the bond energy of the Ti–O bond, which can be attributed to the strong electrostatic interaction between $CsPbBr_3$ and TiO_2.[42–45] Fig. 1d shows the UV-vis diffuse reflectance spectroscopy (DRS) analysis of the samples, which is employed to assess the optical absorption properties. It can be seen that the light absorption edge of blank TiO_2 is around 390 nm, denoting its UV light response nature. After integrating with $CsPbBr_3$, the light absorption of CPB/TiO_2 is extended to approximately 540 nm. Meanwhile, the absorption edge of TiO_2 at 390 nm can also be detected. This should be ascribed to the hybridization of the high weight content of $CsPbBr_3$ with the TiO_2 support. As such, both absorption features are present in the composite. The greatly extended light absorption enables the visible light excitation of the CPB/TiO_2 composites, which is beneficial for promoting solar energy utilization. With the increase of the $CsPbBr_3$ content, the visible light absorption of CPB/TiO_2 is also gradually enhanced (Fig. S3†). Moreover, in comparison with blank $CsPbBr_3$, it is notable that the visible light absorption edge of the hybrid CPB/TiO_2 composite is slightly blue shifted (*ca.* 14 nm). This can be attributed to the quantum size

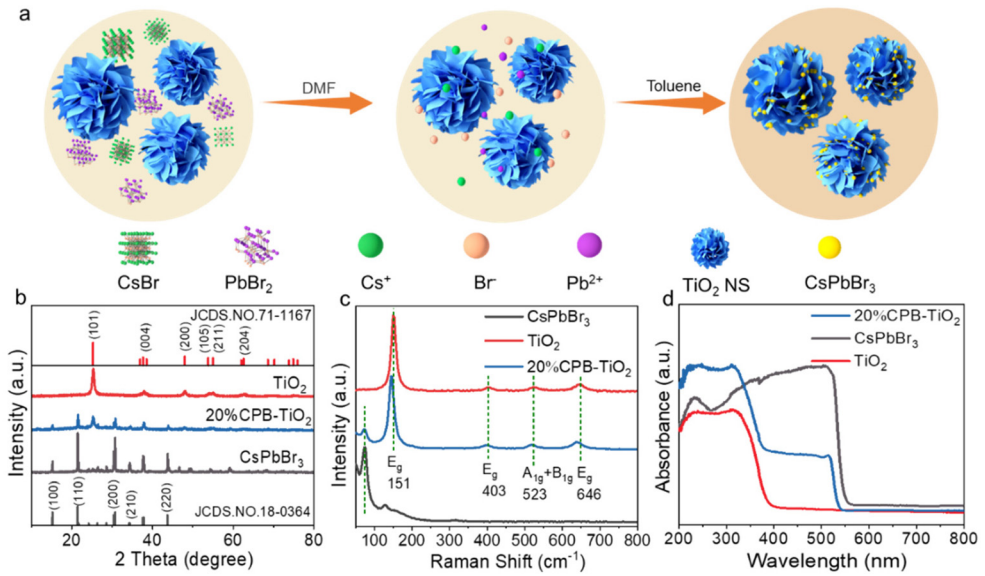

Fig. 1 (a) Schematic diagram of the synthesis of 3D nanoflower-shaped CPB/TiO_2 heterostructure. (b) XRD patterns, (c) Raman spectra, and (d) UV-vis DRS spectra of $CsPbBr_3$, CPB/TiO_2 and TiO_2.

effect resulting from the smaller size of $CsPbBr_3$ in the composite. The inference has been demonstrated by the following scanning electron microscopy (SEM) and transmission electron microscopy (TEM) analyses.

As shown in Fig. 2, Fig. S4 and S5,† SEM is firstly utilized to characterize the morphology and microstructure of the CPB/TiO_2, blank TiO_2 and $CsPbBr_3$ samples. The blank TiO_2 presents a nanoflower shape, which is assembled by vertical nanoflakes (Fig. S4†). The surface of the nanoflake subunits is clean and smooth. For blank $CsPbBr_3$, it shows a large particle morphology and the particle sizes range from 0.9 to 2.0 μm (Fig. S5†). After the construction of the CPB/TiO_2 heterojunction, the TiO_2 nanoflower-shaped structure is maintained (Fig. 2), while the surface of the nanoflake subunits becomes rough due to the *in situ* growth of $CsPbBr_3$. From Fig. 2b–i, it can be clearly seen that for all the CPB/TiO_2 samples, the sizes

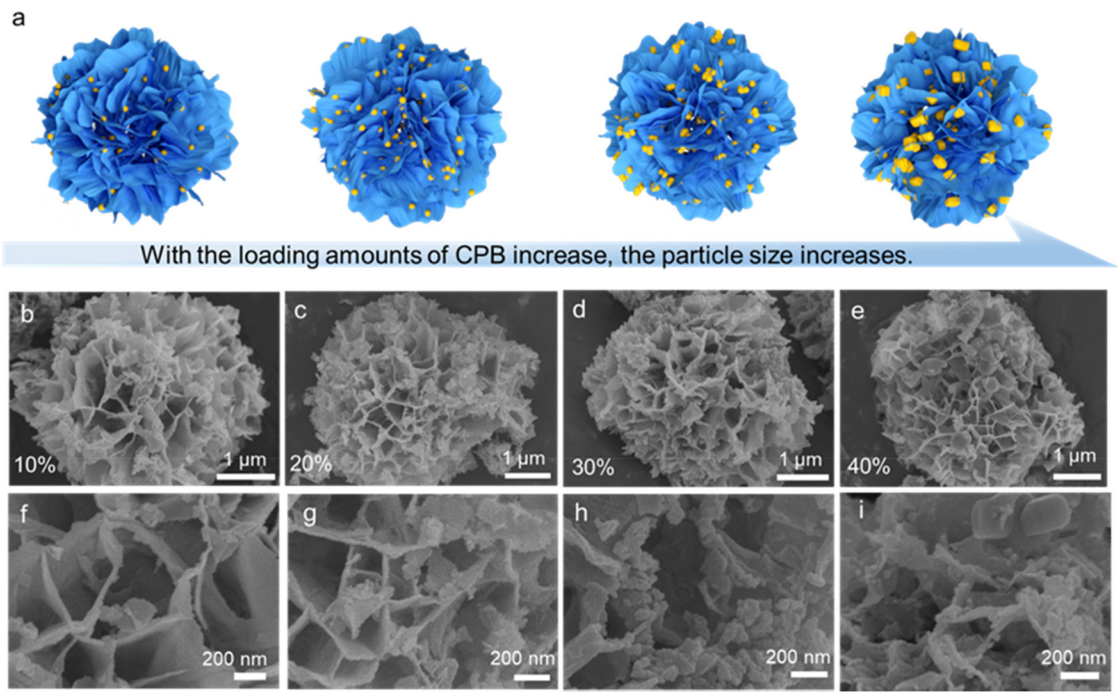

Fig. 2 (a) Schematic and (b–i) SEM images showing the morphology evolution of *x*% CPB/TiO_2 (where *x* = 10, 20, 30, and 40) composites.

of the $CsPbBr_3$ particles in the composites are much smaller than that of blank $CsPbBr_3$, indicating that the formation of a heterojunction is beneficial for preventing the aggregation and reducing the size of the $CsPbBr_3$ halide perovskite. This can be ascribed to the fact that the presence of TiO_2 nanoflowers with nanoflake subunits can act as heterogeneous nucleus sites to facilitate the nucleation and growth of $CsPbBr_3$, which generates more seeds and leads to the smaller size of the $CsPbBr_3$ particles.[20] The significantly decreased particle size could greatly promote the exposure of surface active sites and inhibit the charge recombination of $CsPbBr_3$ under light irradiation. Moreover, it is notable that with the increase of the $CsPbBr_3$ contents from 10% to 40% in the composites, the particle sizes of $CsPbBr_3$ are increased, as schematically illustrated in Fig. 2a. This can be attributed to the further growth of $CsPbBr_3$ at high concentrations.

To further obtain the microscopic structural information of the samples, transmission electron microscopy (TEM) analysis is carried out. Taking 20%CPB/TiO_2 as an example, the TEM image of the sample (Fig. 3a and b) shows a nanoflake structure of TiO_2. The surface is rough and densely covered by small $CsPbBr_3$ nanoparticles. Since the sample for TEM analysis is prepared by strong ultrasonication, the well-defined $CsPbBr_3$ nanoparticles on the 2D nanoflake surface indicate intimate interfacial contact between the two components. Meanwhile, the intensive coverage of $CsPbBr_3$ forms a large contact interface with TiO_2 nanoflakes, which is conducive to the migration of charge carriers across the CPB/TiO_2 heterojunction.[46] Moreover, nanopores can be observed on the CPB/TiO_2, which results from the mesoporous structure of the TiO_2 nanoflakes, as demonstrated by the N_2 adsorption–desorption analysis (Fig. S6†). The high-resolution TEM (HRTEM) image (Fig. 3c) shows distinct lattice fringes of 0.35 nm and 0.41 nm, corresponding to the (101) planes and (110) planes of anatase TiO_2 and monoclinic $CsPbBr_3$, respectively. Furthermore, Fig. 3d shows the corresponding energy dispersive X-ray spectroscopy (EDS) elemental mapping analysis of 20%CPB/TiO_2. Cs, Pb, Br, Ti and O elements are uniformly distributed on the nanoflake structure, indicating that $CsPbBr_3$ and TiO_2 are well combined. The results further verify the formation of CPB/TiO_2 hybrid composite with intimate interfacial contact. Moreover, in comparison with blank TiO_2, the 20%CPB/TiO_2 composite displays a smaller specific surface area (Table S1†), which can be attributed to the fact that the growth of $CsPbBr_3$ nanoparticles on the surface of TiO_2 may aggregate in the TiO_2 pores. Correspondingly, the total pore volume of 20%CPB/TiO_2 is also slightly lower than that of blank TiO_2. The result matches with the SEM measurement.

To study the surface chemical states of the samples, X-ray photoelectron spectroscopy (XPS) has been performed. As shown in Fig. 4a, the presence of Cs, Pb, Br, O and Ti elements can be detected from the XPS survey spectrum of CPB/TiO_2. The high-resolution spectrum of Ti 2p shows two peaks of Ti $2p_{3/2}$ and Ti $2p_{1/2}$ at 458.5 eV and 464.2 eV (Fig. 4b), which indicates that Ti element mainly exists as Ti^{4+} ions. For the O 1s pattern (Fig. 4c), it can be divided into two peaks, which are attributed to the lattice O (Ti–O) and hydroxyl O (–OH). Fig. S7† shows the fine-scanned Cs 3d XPS spectrum, and the two peaks with binding energies at 724.2 eV and 738.1 eV are assigned to Cs $3d_{5/2}$ and Cs $3d_{3/2}$, indicating that the chemical state of the Cs in the composite is +1. The Pb 4f spectrum in Fig. 4d shows characteristic peaks at 138.0 eV and 142.9 eV, corresponding to Pb $4f_{7/2}$ and Pb $4f_{5/2}$ orbitals of Pb^{2+} ion. Moreover, the Br 3d is decomposed into two peaks at 67.9 eV and 68.9 eV, corresponding to the binding energies of Br $3d_{5/2}$ and $3d_{3/2}$, attributed to the presence of Br^- (Fig. 4e). It is worth noting that for the CPB/TiO_2 composite, the Ti 2p and O

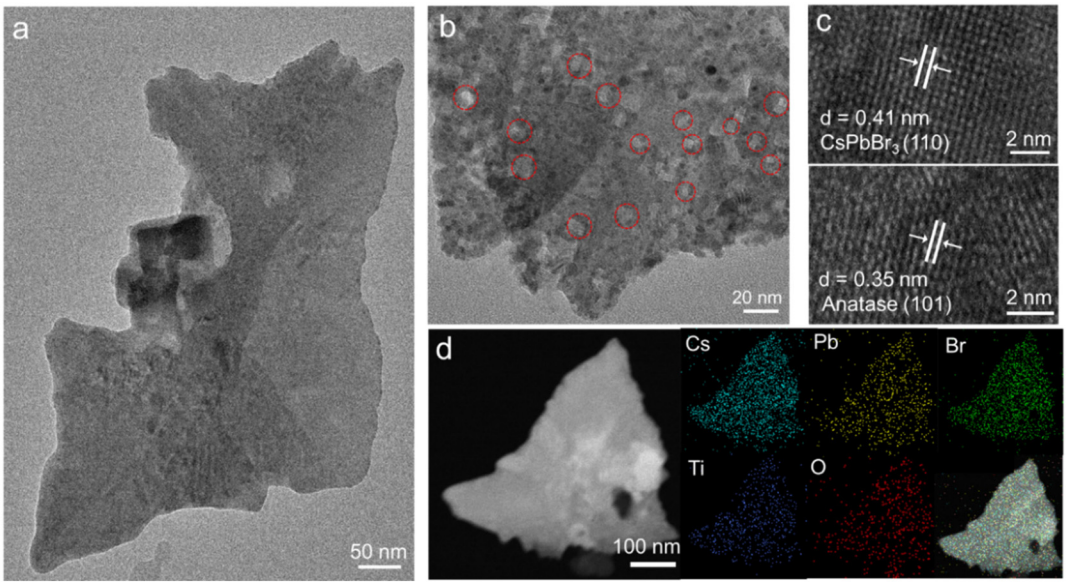

Fig. 3 (a and b) TEM images, (c) HRTEM image, and (d) corresponding EDS elemental mapping images of 20%CPB/TiO_2.

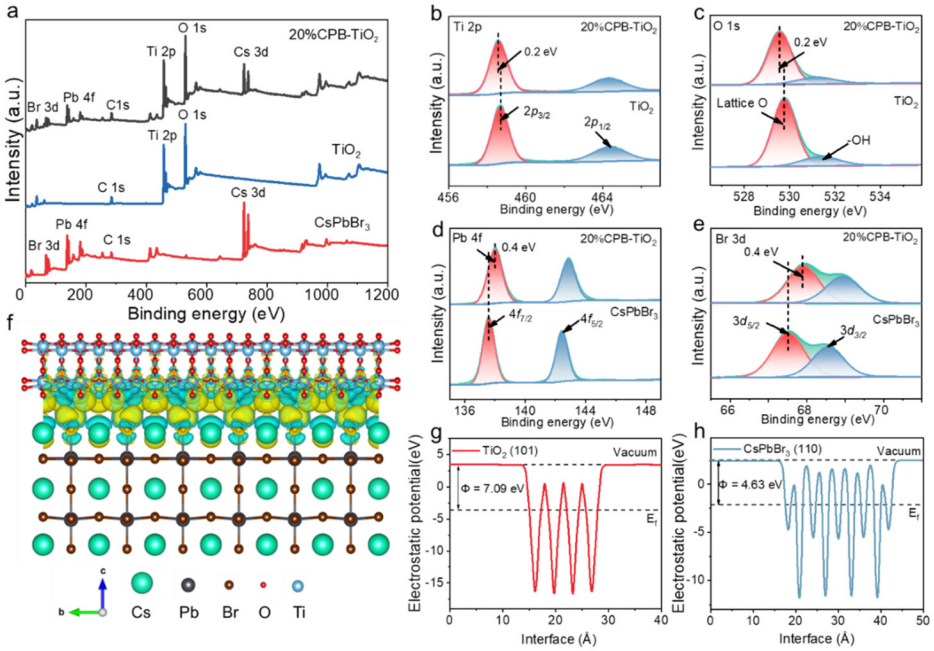

Fig. 4 XPS spectra of $CsPbBr_3$, TiO_2 and 20%CPB/TiO_2: (a) survey, (b) Ti 2p, (c) O 1s, (d) Pb 4f and (e) Br 3d. (f) Charge density differences in the CPB/TiO_2 composite. (g and h) The work functions of blank TiO_2 and $CsPbBr_3$.

1s peaks show a negative shift of 0.2 eV in comparison with blank TiO_2 (Fig. 4b and c). In contrast, the binding energies of Cs 4d, Pb 4f, and Br 3d in the CPB/TiO_2 show a positive shift (Fig. 4d and e and S7†), which are higher than those of blank $CsPbBr_3$ by 0.4 eV. The results verify the strongly interacted interface with electron transfer from the $CsPbBr_3$ to the TiO_2 nanosheets in the heterostructure, which is in accordance with the Raman analysis. To further clarify the interaction and electron transfer at the interface, density functional theory (DFT) calculations have been carried out. Fig. 4g and h shows the work functions of the TiO_2 (101) and $CsPbBr_3$ (110) slabs, which are 7.09 eV and 4.63 eV, respectively, corresponding to the Fermi levels (E_f) of −3.61 eV and −2.51 eV (*vs.* the vacuum level). Due to the lower E_f value of TiO_2 than that of blank $CsPbBr_3$, the electrons would be migrated from $CsPbBr_3$ to TiO_2 at the heterojunction interface until their E_f are aligned. A similar result is obtained from the calculated planar-averaged charge density difference of CPB/TiO_2. As shown in Fig. 4f, the light cyan and yellow regions indicate the charge depletion and accumulation area, respectively. The calculation results reveal that the cyan region is mainly on the $CsPbBr_3$ side, while the yellow region is on the TiO_2 side, further validating the transfer of electrons from $CsPbBr_3$ to TiO_2. This is consistent with the XPS analysis results.

Photocatalytic performances

Collectively, the above characterization faithfully verifies the successful fabrication of CPB/TiO_2 hybrid composites with intimate interfacial contact and strong chemical interaction. The presence of TiO_2 nanoflower with 2D nanoflake subunits greatly inhibits the agglomeration of the halide perovskites, while $CsPbBr_3$ extends the light absorption range of TiO_2. In view of the desired structural and optical properties, the photocatalytic oxidation of toluene over the hybrid CPB/TiO_2 composites has been tested. A 300 W xenon lamp equipped with a 420 nm cutoff filter is utilized as a visible light source. It is well known that the solvent/reactant ratio has great influence on the oxidation of toluene,[2,47] and thus, the reaction condition of different acetonitrile/toluene ratio is firstly optimized using 20%CPB/TiO_2 as an example. As shown in Fig. 5a, as the ratio of toluene increases from 0.3 to 1 mL, the photoactivity of the 20%CPB/TiO_2 composite gradually increases. The catalyst shows the highest toluene conversion rate of 10 200 μmol g^{-1} h^{-1} when the volume ratio of acetonitrile solvent and toluene reactant is 2 : 1. The enhanced photoactivity can be attributed to the fact that the increased toluene concentration enhances the reaction possibility between the photogenerated charge carriers and the toluene molecules. However, further increase of toluene to 1.5 mL and 2 mL decreases the conversion rate. This might be ascribed to the excess adsorption of the toluene reactant on the catalyst surface, which would slow down the desorption of the BA and BAD products and suppress the oxidation activity.[48] Based on the result, the following photoactivity tests of all the other samples are carried out under the optimized condition with a acetonitrile/toluene ratio of 2 : 1.

Fig. 5b shows the visible-light-driven photocatalytic performances of the blank $CsPbBr_3$ and CPB/TiO_2 composites with different ratios of CPB for the selective oxidation of toluene. The blank $CsPbBr_3$ exhibits a low activity with generation rates of 390 μmol g^{-1} h^{-1} for BAD and 130 μmol g^{-1} h^{-1} for BA. The unsatisfactory photocatalytic performance should

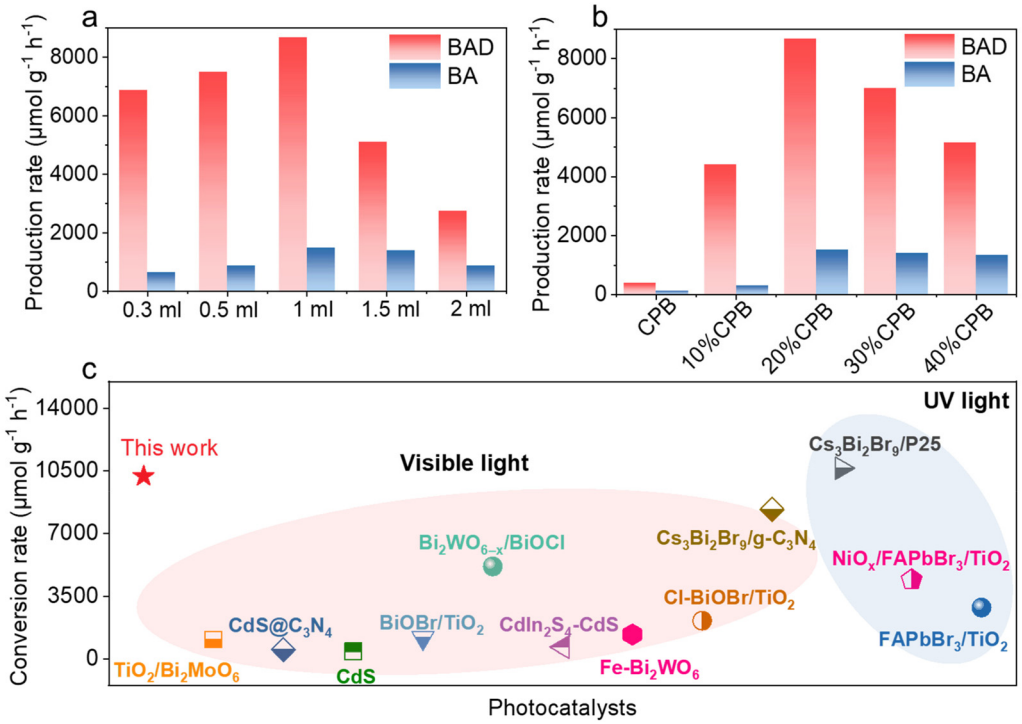

Fig. 5 (a) Photocatalytic oxidation of toluene with different toluene amounts in acetonitrile solvent over 20%CPB/TiO_2. The total volume is 3 ml. (b) Photocatalytic oxidation of toluene over blank TiO_2, CPB/TiO_2 composite and blank $CsPbBr_3$. (c) Performance comparison with reported photocatalysts for UV and visible-light-driven selective oxidation of toluene.

be due to the severe charge recombination caused by the large particle size of $CsPbBr_3$. For blank TiO_2, it presents no activity. This is reasonable since the TiO_2 has no visible light absorption and cannot be excited by visible light. In contrast, after the hybridization of $CsPbBr_3$ with TiO_2, the photocatalytic performances of all the hierarchical CPB/TiO_2 heterojunctions are significantly improved. The best photocatalytic toluene oxidation activity is achieved over the 20%CPB/TiO_2 composite, which shows a toluene conversion rate of 10 200 μmol g^{-1} h^{-1} (with a BAD production rate of 8670 μmol g^{-1} h^{-1} and a BA generation rate of 1530 μmol g^{-1} h^{-1}). The photoactivity is about 20 times higher than that of blank $CsPbBr_3$, which is also among the top photocatalytic performances reported so far for UV and visible-light-driven selective oxidation of toluene (Fig. 5c and Table S2†). The apparent quantum efficiency (AQE) of the 20%$CsPbBr_3$/TiO_2 composite reaches 2.9% at λ = 420 nm for the transformation of toluene into BA and BAD (Fig. S14†). The gas chromatography-mass spectrometry (GC-MS) analysis of the reaction solution after light irradiation reveals four peaks, which are ascribed to the acetonitrile solvent, toluene reactant, BAD and BA products (Fig. S8†). No other product or intermediate is detected, validating the high selectivity of the reaction. With the increase of $CsPbBr_3$ loading to higher contests (30% and 40%), it results in a performance degradation. This may be ascribed to the fact that: (1) an excess of halide perovskite tends to aggregate into large particles, which will lead to longer migration distances of charge carriers and increase charge recombination; (2) the coverage of excessive and oversized $CsPbBr_3$ on the TiO_2 surface will lead to the reduction of the exposed surface area, inhibiting the adsorption of toluene molecules.

Furthermore, the broad applicability of the CPB/TiO_2 photocatalyst is investigated for the photocatalytic selective oxidation of C(sp^3)–H of toluene derivatives with different substituents. As shown in Table 1, these aromatics are efficiently converted into the corresponding aldehydes and alcohols. The selectivity for the aldehyde product is higher than 70%. Notably, the substrate with electron-withdrawing substituents (–F, –Cl, and –Br) displays lower photocatalytic activity. This can be attributed to the fact that the electron-withdrawing groups on the benzene ring inhibit the abstraction of hydrogen from the methyl group.[49,50] In addition, *p*-xylene shows a higher toluene conversion rate (12 746 μmol g^{-1} h^{-1}) than its isomers of *o*-xylene (9900 μmol g^{-1} h^{-1}) and *m*-xylene (10 930 μmol g^{-1} h^{-1}), which can be attributed to the steric hindrance of the methyl groups hindering the reactant adsorption and activation on the catalyst surface.[51,52]

Moreover, the cycle test of the 20%$CsPbBr_3$/TiO_2 has been carried out. After repeating the photoactivity test for 4 cycles (Fig. S16†), the catalyst still maintains a high activity with negligible decrease in the conversion rate of toluene. In addition, the used 20%$CsPbBr_3$/TiO_2 has been further characterized by XRD and XPS (Fig. S17 and S18†). No obvious change in the crystal structure and surface chemical state is observed for the composite before and after the reaction. These results indicate the high stability of the $CsPbBr_3$/TiO_2 composite.

Table 1 Photocatalytic oxidation of C(sp^3)–H in substituted toluene over 20%CPB/TiO_2[a]

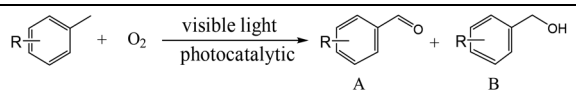

Entry	Substrates	Conversion rate (μmol g^{-1} h^{-1})	Selectivity (%) A	B
1		10 200	85	15
2		5950	83	17
3	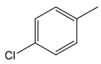	9040	88	12
4		9770	87	13
5		9900	76	24
6		10 930	72	28
7		12 746	71	29

[a] Reaction conditions: catalyst (10 mg 20%CPB/TiO_2), substrate (1 mL), MeCN (2 mL), 1 atm of O_2, 2 h irradiation with visible light (λ > 420 nm).

Photoelectric properties

In order to better understand the reasons for the improved photocatalytic performance, the band structures of the $CsPbBr_3$ and the TiO_2 are investigated using Mott–Schottky (M–S) measurements and the DRS analysis. As shown in Fig. 6a and b, the positive slopes indicate that $CsPbBr_3$ and TiO_2 are typical n-type semiconductors.[53] The flat band potentials (E_{FB}) are calculated to be −0.86 V and −0.34 V (*vs.* NHE) for $CsPbBr_3$ and TiO_2, respectively. Usually, the conduction band potential (E_{CB}) for an n-type semiconductor is more negative of about 0.1 eV than that of E_{FB}.[54] Thus, the E_{CB} values of $CsPbBr_3$ and TiO_2 are determined to be −0.96 V and −0.44 V (*vs.* NHE), respectively. In addition, the corresponding bandgaps of TiO_2 and $CsPbBr_3$ are estimated by Tauc plots transformed from the DRS spectra (Fig. S9†), which are 3.20 eV and 2.28 eV, respectively. Based on these, the valence band positions (E_{VB}) of $CsPbBr_3$ and TiO_2 are calculated to be 1.32 V and 2.76 V. As a result, a type-II heterojunction is formed between $CsPbBr_3$ and TiO_2 because of the staggered band structures.

To study the influence of the heterojunction structure on the transfer behavior of photogenerated charge carriers, transient photocurrent and electrochemical impedance spectra (EIS) tests are performed. As shown in Fig. 6c, under visible light irradiation, both $CsPbBr_3$ and CPB/TiO_2 show rapid and stable photocurrent responses, while TiO_2 does not. This can be

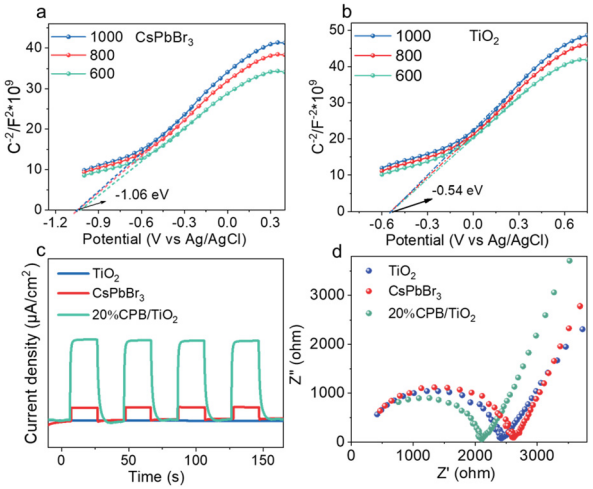

Fig. 6 (a and b) M–S plots of $CsPbBr_3$ and TiO_2. (c) Transient photocurrent responses, and (d) EIS Nyquist plots of blank TiO_2, $CsPbBr_3$ and the CPB/TiO_2 composite.

attributed to the inability of TiO_2 to be excited by visible light (Fig. 1d). The photocurrent intensity of blank $CsPbBr_3$ is markedly lower than that of 20% CPB/TiO_2. This should be due to the agglomerated large particle size of the blank $CsPbBr_3$, which leads to a severe recombination of photogenerated charge carriers.[54] Moreover, Fig. 6d shows the Nyquist plots of the samples, which is employed to investigate the interfacial charge transfer efficiency.[55] In general, the smaller diameter of the semicircular arc in the Nyquist plots reflects the lower electron transfer resistance. It can be found that the 20%CPB/TiO_2 sample has the minimum arc radius, which means the best electronic conductivity and charge separation ability.[56,57] Furthermore, the steady-state photoluminescence (PL) spectra are also used to examine the charge separation efficiency. As shown in Fig. S19,† the 20%$CsPbBr_3$/TiO_2 composite shows a much lower PL intensity than that of $CsPbBr_3$, revealing that the charge recombination is significantly suppressed in the composite. In addition, the TiO_2 shows no obvious PL signal. This is in accordance with the photocurrent analysis that the TiO_2 is unable to be excited to generate charge carriers by visible light. These photoelectrochemical findings highlight that the construction of the type-II heterojunction between $CsPbBr_3$ and TiO_2 could effectively accelerate charge transfer, thus contributing to improving the photocatalytic performance.

Furthermore, for heterogeneous photocatalytic reactions, the effective adsorption of the reactant on the catalyst surface is another requisite for the ignition of the redox reaction.[23,58–60] The BET surface area and porous structure analyses of the TiO_2, $CsPbBr_3$ and 20%CPB/TiO_2 samples have shown that the introduction of TiO_2 nanoflower significantly improves the specific surface area and pore volume of 20% CPB/TiO_2 in comparison with that of blank TiO_2 (Fig. S6 and Table S1†). Generally, a larger specific surface area and a porous structure enable better adsorption capacity, and

exposure of more active sites of catalysts. To further reveal the contribution of the heterostructure for the reactant adsorption, Fourier transform infrared (FTIR) spectroscopy is used to identify the adsorbed toluene species on the $CsPbBr_3$, TiO_2 and 20%CPB/TiO_2 surface. As shown in Fig. 7a, for all three samples after adsorption equilibrium, the typical absorption peaks of toluene are observed, including the C–H stretching vibration of the aromatic ring at 3083 and 3038 cm^{-1}, the skeleton vibration of the aromatic ring at 1606 and 1495 cm^{-1}, and the C–H symmetric and asymmetric stretching of the methylene group at 2934 and 2875 cm^{-1}.[61,62] Notably, the signal of toluene molecules of 20%CPB/TiO_2 is obviously higher than that of blank $CsPbBr_3$, yet is lower than that of blank TiO_2. The result indicates that the introduction of TiO_2 can promote the toluene adsorption capacity of CPB/TiO_2, which is conducive to the catalytic conversion.

Finally, to investigate the influence of the hierarchical flower-like nanostructure constructed using 2D nanoflake subunits on the photocatalytic performance, a collapsed 20%CPB/TiO_2 catalyst (marked as 20%CPB/TiO_2–C) without such structure has been fabricated for comparison. As shown in Fig. 7b, the photoactivity test reveals that the 20%CPB/TiO_2–C has a BAD generation rate of 6000 μmol g^{-1} h^{-1} and a BA production rate of 1250 μmol g^{-1} h^{-1}, which is notably lower than the CPB/TiO_2 catalyst. Fig. S10† shows the morphology analysis of the 20%CPB/TiO_2–C catalyst, which reveals a bulky grain structure with a rough surface. $CsPbBr_3$ nanoparticles are dispersed on the surface of the massive TiO_2. The size of the $CsPbBr_3$ particles in the composite is also much smaller than that of blank $CsPbBr_3$, which once again proves that TiO_2 plays a critical role in inhibiting the growth of $CsPbBr_3$. Nevertheless, compared with 20%CPB/TiO_2, the size of the $CsPbBr_3$ particles is much larger in the 20%CPB/TiO_2–C catalyst. The result indicates that the TiO_2 nanoflakes are more beneficial for preventing the agglomeration of the $CsPbBr_3$ particles.

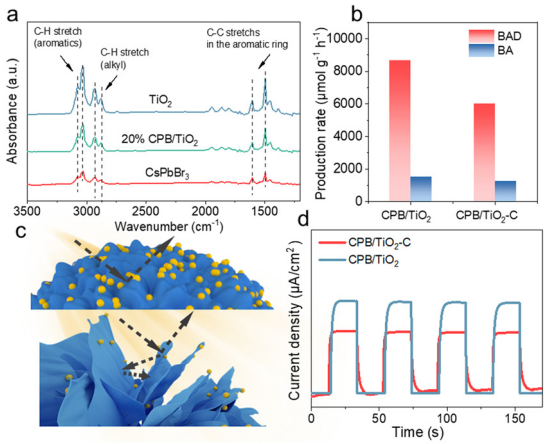

Fig. 7 (a) FTIR spectra of 20%CPB/TiO_2, TiO_2 and $CsPbBr_3$ after adsorption of saturated toluene. (b) Photoactivity comparison between CPB/TiO_2 and CPB/TiO_2–C. (c) Schematic diagram of light absorption over CPB/TiO_2 and CPB/TiO_2–C. (d) Transient photocurrent responses of CPB/TiO_2 and CPB/TiO_2–C.

In addition, UV-vis DRS is performed to study the optical absorption property of the 20%CPB/TiO_2–C catalyst. The sample shows a similar absorption edge as that of 20%CPB/TiO_2, but the light absorption intensity in the range of 200–550 nm is lower (Fig. S11†). The result indicates that the 3D hierarchical CPB/TiO_2 structure is more efficient for solar energy collection, which can be attributed to the multiple light reflection and refraction caused by the vertical nanoflakes, as schematically illustrated in Fig. 7c. Meanwhile, the transient photocurrent response test shows that the 20%CPB/TiO_2 catalyst exhibits a higher photocurrent density than that of CPB/TiO_2–C under visible light irradiation, indicating more efficient charge transfer (Fig. 7d). This can be related to the fact that TiO_2 nanoflakes facilitate the formation of smaller $CsPbBr_3$ particle, which could shorten the charge transfer distance to the surface and promote the interfacial charge separation. Hence, to sum up, the construction of the unique hierarchical CPB/TiO_2 structure greatly enhances the photocatalytic performance due to the existence of TiO_2 nanoflakes, which (1) greatly prohibits the aggregation of $CsPbBr_3$, forming much smaller perovskite particles that shorten the charge transfer distance; (2) increases light absorption by multiple reflection and scattering between the nanoflakes structure that benefits the solar energy harvesting and conversion; (3) enhances the adsorption of toluene molecules and promotes the surface reaction rates.

Photocatalytic mechanism

To elucidate the photocatalytic mechanism of toluene oxidation over the CPB/TiO_2 photocatalyst, a series of control experiments have been conducted in the absence of O_2 or with the addition of specific radical scavengers. As shown in Fig. 8a, toluene oxidation is almost completely suppressed when O_2 is replaced by Ar, indicating that O_2 is indispensable. When isopropanol (IPA) is added into the reaction system as a scavenger of hydroxyl radicals ($^{\bullet}OH$), it has almost no effect on toluene conversion, suggesting that $^{\bullet}OH$ is rarely involved in the reaction. In contrast, whether adding ammonium oxalate (AO) to eliminate holes (h^+) or butylated hydroxytoluene (BHT) to capture carbon-centered radicals, the reaction rate significantly reduces. Besides, the toluene conversion is also significantly decreased when BQ is added as a superoxide free radical ($^{\bullet}O_2^-$) scavenger. The above results clearly indicate that $^{\bullet}O_2^-$, h^+, and carbon-centered radicals play key roles in the photocatalytic selective oxidation of toluene.

Subsequently, to further identify the existence of $^{\bullet}O_2^-$, electron paramagnetic resonance (EPR) spectroscopy was employed using 5,5-dimethyl-pyrroline-*N*-oxide (DMPO) as a trapping agent. As shown in Fig. S12† and Fig. 8b, no DMPO-$^{\bullet}O_2^-$ signal is detected under dark conditions. After visible light irradiation, distinct signals of DMPO-$^{\bullet}O_2^-$ are observed for both $CsPbBr_3$ and CPB/TiO_2, while no signals are detected from TiO_2. The CPB/TiO_2 catalyst exhibits a higher ability to generate more $^{\bullet}O_2^-$ radicals than that of pure $CsPbBr_3$, which is important to promote the oxidation of toluene. Moreover, no DMPO-$^{\bullet}OH$ signal is observed under the

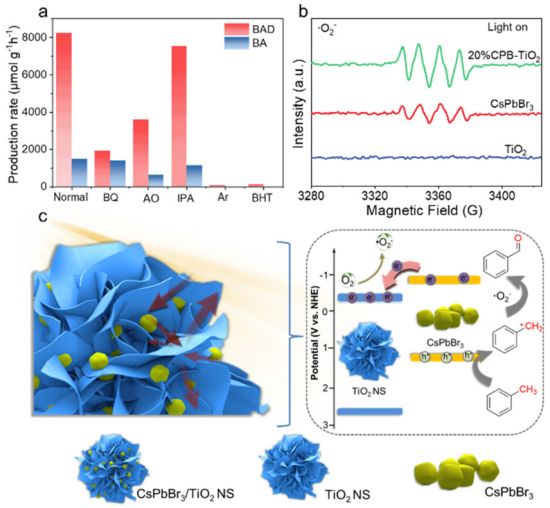

Fig. 8 (a) Photocatalytic toluene oxidation in the absence or presence of various radical scavengers. (b) EPR spectra of DMPO-$^{\bullet}O_2^-$. (c) Schematic illustration of the proposed mechanism of photocatalytic oxidation of toluene over the CPB/TiO_2 composite.

same conditions, demonstrating that $^{\bullet}OH$ is absent in the reaction process (Fig. S13 and S15†).

Based on the above analyses, a possible photocatalytic reaction mechanism over the hierarchical CPB/TiO_2 heterojunction is proposed. As schematically illustrated in Fig. 8c, upon photoexcitation, electrons and holes are generated in the conduction band (CB) and the valence band (VB) of $CsPbBr_3$. Due to the staggered energy bands, the photogenerated electrons in the CB of $CsPbBr_3$ can efficiently migrate towards the CB of TiO_2 and left holes on the VB of $CsPbBr_3$, which prolongs the lifetime of the photogenerated charge carriers. After that, molecular O_2 can be activated by electrons on the CB of TiO_2. Meanwhile, photogenerated holes oxidize the toluene to produce benzyl radicals ($^{\bullet}CH_2$–R) on the VB of $CsPbBr_3$. Then, the $^{\bullet}O_2^-$ radical reacts with the benzyl radicals to produce benzaldehyde.

Conclusions

In summary, we have designed and synthesized a hierarchical CPB/TiO_2 heterojunction as an advanced photocatalyst for efficient visible-light-driven toluene oxidation by assembling $CsPbBr_3$ nanoparticles onto nanoflower-shaped TiO_2 with 2D nanoflake subunits. The formed CPB/TiO_2 composite integrates the structural and electronical merits of the nanoflower-shaped TiO_2 and halide perovskite $CsPbBr_3$, which not only enhances solar light utilization, but also enhances the adsorption of the toluene reactant, and boosts the separation and transportation of photogenerated carriers. A high toluene oxidation rate of 10 200 μmol g^{-1} h^{-1} is achieved over the optimal CPB/TiO_2 composite, which is about 20-fold higher than that of blank $CsPbBr_3$. The study demonstrates the significance of rational design of well-defined hierarchical heterojunction catalysts over metal halide perovskites for efficient photocatalytic redox reactions.

Conflicts of interest

There are no conflicts to declare.

Acknowledgements

This work was financially supported by the National Key Research and Development Program of China (2019YFC1908203), the National Natural Science Foundation of China (22178057 and 21905049), the Natural Science Foundation of Fujian Province (2020J01201 and 2021J01197), the Research Foundation of the Academy of Carbon Neutrality of Fujian Normal University (TZH2022-07), and the Award Program for Minjiang Scholar Professorship.

References

1 W. Wu, G. Zhang, J. Zhang, G. Wang, C.-H. Tung and Y. Wang, *Chem. Eng. J.*, 2021, **404**, 126433.
2 X. Li, T. Wang, X. Tao, G. Qiu, C. Li and B. Li, *J. Mater. Chem. A*, 2020, **8**, 17657–17669.
3 S. Okunaka, H. Tokudome and Y. Hitomi, *J. Catal.*, 2020, **391**, 480–484.
4 S. Zhang, W. Huang, X. Fu, X. Zheng, S. Meng, X. Ye and S. Chen, *Appl. Catal., B*, 2018, **233**, 1–10.
5 J. Li, B. Ren, X. Yan, P. Li, S. Gao and R. Cao, *J. Catal.*, 2021, **395**, 227–235.
6 C. Xu, F. Yang, B. Deng, Y. Zhuang, D. Li, B. Liu, W. Yang and Y. Li, *J. Catal.*, 2020, **383**, 1–12.
7 J. Li, S. Zhang, S. Gui, G. Chen, Y. Wang, Z. Wang, X. Zheng, S. Meng, C. Ruan and S. Chen, *Appl. Surf. Sci.*, 2023, **611**, 155616.
8 Q. Zhang, J. Wang, X. Ye, Z. Hui, L. Ye, X. Wang and S. Chen, *ACS Appl. Mater. Interfaces*, 2019, **11**, 46735–46745.
9 Y. Liu, L. Chen, Q. Yuan, J. He, C. T. Au and S. F. Yin, *Chem. Commun.*, 2016, **52**, 1274–1277.
10 M. Zhou, S. Li, S. Wang, Z. Jiang, C. Yang, F. Guo, X. Wang and W.-K. Ho, *Appl. Surf. Sci.*, 2022, **599**, 153985.
11 M. Zhang, W. Sun, H. Lv and Z.-H. Zhang, *Curr. Opin. Green Sustainable Chem.*, 2021, **27**, 100390.
12 Z. Zhang, Y. Liang, H. Huang, X. Liu, Q. Li, L. Chen and D. Xu, *Angew. Chem., Int. Ed.*, 2019, **58**, 7263–7267.
13 M. Zhang, Z. Li, X. Xin, J. Zhang, Y. Feng and H. Lv, *ACS Catal.*, 2020, **10**, 14793–14800.
14 T. Chen, B. Weng, S. Lu, H. Zhu, Z. Chen, L. Shen, M. B. J. Roeffaers and M. Q. Yang, *J. Phys. Chem. Lett.*, 2022, **13**, 6559–6565.
15 R. Cheng, J. A. Steele, M. B. J. Roeffaers, J. Hofkens and E. Debroye, *ACS Appl. Energy Mater.*, 2021, **4**, 3460–3468.

16 H. Huang, J. Zhao, Y. Du, C. Zhou, M. Zhang, Z. Wang, Y. Weng, J. Long, J. Hofkens, J. A. Steele and M. B. J. Roeffaers, *ACS Nano*, 2020, **14**, 16689–16697.
17 H. Huang, H. Yuan, J. Zhao, G. Solís-Fernández, C. Zhou, J. W. Seo, J. Hendrix, E. Debroye, J. A. Steele, J. Hofkens, J. Long and M. B. J. Roeffaers, *ACS Energy Lett.*, 2018, **4**, 203–208.
18 H. Huang, H. Yuan, K. P. F. Janssen, G. Solís-Fernández, Y. Wang, C. Y. X. Tan, D. Jonckheere, E. Debroye, J. Long, J. Hendrix, J. Hofkens, J. A. Steele and M. B. J. Roeffaers, *ACS Energy Lett.*, 2018, **3**, 755–759.
19 C. Chen, J. Zhou, J. Geng, R. Bao, Z. Wang, J. Xia and H. Li, *Appl. Surf. Sci.*, 2020, **503**, 144287.
20 Y. Dai, C. Poidevin, C. Ochoa-Hernandez, A. A. Auer and H. Tuysuz, *Angew. Chem., Int. Ed.*, 2020, **59**, 5788–5796.
21 F. Xu, K. Meng, B. Cheng, S. Wang, J. Xu and J. Yu, *Nat. Commun.*, 2020, **11**, 4613.
22 M.-Q. Yang, J. Dan, S. J. Pennycook, X. Lu, H. Zhu, Q.-H. Xu, H. J. Fan and G. W. Ho, *Mater. Horiz.*, 2017, **4**, 885–894.
23 X. Lin, Z. Xie, B. Su, M. Zheng, W. Dai, Y. Hou, Z. Ding, W. Lin, Y. Fang and S. Wang, *Nanoscale*, 2021, **13**, 18070–18076.
24 S. Wang, B. Y. Guan and X. W. Lou, *Energy Environ. Sci.*, 2018, **11**, 306–310.
25 L. Zhu, M. Hong and G. W. Ho, *Nano Energy*, 2015, **11**, 28–37.
26 L. He, W. Zhang, K. Zhao, S. Liu and Y. Zhao, *J. Mater. Chem. A*, 2022, **10**, 4758–4769.
27 Q. Shen, S. Zhou, F.-L. Yang, X. Wang and X. Han, *J. Mater. Chem. A*, 2022, **10**, 4974–4980.
28 S. Wang, B. Y. Guan, X. Wang and X. W. D. Lou, *J. Am. Chem. Soc.*, 2018, **140**, 15145–15148.
29 S. Wang, B. Y. Guan and X. W. D. Lou, *J. Am. Chem. Soc.*, 2018, **140**, 5037–5040.
30 T. Zhu, L. Zhu, J. Wang and G. W. Ho, *J. Mater. Chem. A*, 2016, **4**, 13916–13922.
31 Z. Chen, F. Guo, H. Sun, Y. Shi and W. Shi, *J. Colloid Interface Sci.*, 2022, **607**, 1391–1401.
32 K. Lan, Y. Liu, W. Zhang, Y. Liu, A. Elzatahry, R. Wang, Y. Xia, D. Al-Dhayan, N. Zheng and D. Zhao, *J. Am. Chem. Soc.*, 2018, **140**, 4135–4143.
33 Q. Sun, W. Ye, J. Wei, L. Li, J. Wang, J.-H. He and J.-M. Lu, *J. Alloys Compd.*, 2022, **893**, 162326.
34 J. Hafner, *J. Comput. Chem.*, 2008, **29**, 2044–2078.
35 G. Kresse and J. Hafner, *Phys. Rev. B: Condens. Matter Mater. Phys.*, 1993, **48**, 13115–13118.
36 L. Rao, Y. Tang, C. Yan, J. Li, G. Zhong, K. Tang, B. Yu, Z. Li and J. Z. Zhang, *J. Mater. Chem. C*, 2018, **6**, 5375–5383.
37 J. Liu, L. Zhu, S. Xiang, Y. Wei, M. Xie, H. Liu, W. Li and H. Chen, *Sustainable Energy Fuels*, 2019, **3**, 184–194.
38 G. Gao, Q. Xi, H. Zhou, Y. Zhao, C. Wu, L. Wang, P. Guo and J. Xu, *Nanoscale*, 2017, **9**, 12032–12038.
39 L. Zhang, Q. Zeng and K. Wang, *J. Phys. Chem. Lett.*, 2017, **8**, 3752–3758.
40 X. Mo, X. Li, G. Dai, P. He, J. Sun, H. Huang and J. Yang, *Nanoscale*, 2019, **11**, 21386–21393.
41 D. M. Calistru, L. Mihut, S. Lefrant and I. Baltog, *J. Appl. Phys.*, 1997, **82**, 5391–5395.
42 H. J. Kong, D. H. Won, J. Kim and S. I. Woo, *Chem. Mater.*, 2016, **28**, 1318–1324.
43 I.-S. Cho, D. W. Kim, S. Lee, C. H. Kwak, S.-T. Bae, J. H. Noh, S. H. Yoon, H. S. Jung, D.-W. Kim and K. S. Hong, *Adv. Funct. Mater.*, 2008, **18**, 2154–2162.
44 S. K. Lakhera, H. Y. Hafeez, R. Venkataramana, P. Veluswamy, H. Choi and B. Neppolian, *Appl. Surf. Sci.*, 2019, **487**, 1289–1300.
45 J. Yu and A. Kudo, *Adv. Funct. Mater.*, 2006, **16**, 2163–2169.
46 C. Q. Li, X. Du, S. Jiang, Y. Liu, Z. L. Niu, Z. Y. Liu, S. S. Yi and X. Z. Yue, *Adv. Sci.*, 2022, **9**, e2201773.
47 J. Kou, C. Lu, J. Wang, Y. Chen, Z. Xu and R. S. Varma, *Chem. Rev.*, 2017, **117**, 1445–1514.
48 J. Wu, Y. Wang, S. Zhang, Y. Liu and F. Wang, *Appl. Catal., B*, 2023, **332**, 122741.
49 H. Han, X. Zheng, C. Qiao, Z. Xia, Q. Yang, L. Di, Y. Xing, G. Xie, C. Zhou, W. Wang and S. Chen, *ACS Catal.*, 2022, **12**, 10668–10679.
50 R. Yuan, S. Fan, H. Zhou, Z. Ding, S. Lin, Z. Li, Z. Zhang, C. Xu, L. Wu, X. Wang and X. Fu, *Angew. Chem., Int. Ed.*, 2013, **52**, 1035–1039.
51 W. Sheng, X. Wang, Y. Wang, S. Chen and X. Lang, *ACS Catal.*, 2022, **12**, 11078–11088.
52 X. Li, S. Lyu and X. Lang, *Environ. Res.*, 2021, **195**, 110851.
53 Z. Dong, Z. Zhang, Y. Jiang, Y. Chu and J. Xu, *Chem. Eng. J.*, 2022, **433**, 133762.
54 X. Li, S. Lu, J. Yi, L. Shen, Z. Chen, H. Xue, Q. Qian and M. Q. Yang, *ACS Appl. Mater. Interfaces*, 2022, **14**, 25297–25307.
55 W. Liao, W. Chen, S. Lu, S. Zhu, Y. Xia, L. Qi, M. Q. Yang and S. Liang, *ACS Appl. Mater. Interfaces*, 2021, **13**, 38239–38247.
56 T. Shan, L. Luo, T. Chen, L. Deng, M. Li, X. Yang, L. Shen and M.-Q. Yang, *Green Chem.*, 2023, **25**, 2745–2756.
57 M. Q. Yang, C. F. Tan, W. Lu, K. Zeng and G. W. Ho, *Adv. Funct. Mater.*, 2020, **30**, 2004460.
58 J. Wang, Z. Wang, J. Zhang, S. P. Chai, K. Dai and J. Low, *Nanoscale*, 2022, **14**, 18087–18093.
59 L. Liu, Z. Wang, J. Zhang, O. Ruzimuradov, K. Dai and J. Low, *Adv. Mater.*, 2023, **35**, e2300643.
60 S. Lu, B. Weng, A. Chen, X. Li, H. Huang, X. Sun, W. Feng, Y. Lei, Q. Qian and M.-Q. Yang, *ACS Appl. Mater. Interfaces*, 2021, **13**, 13044–13054.
61 J. Wang, J. Li, W. Yang, Y. Liu, H. Wang, Q. Geng and F. Dong, *Appl. Catal., B*, 2021, **297**, 120489.
62 X. Zhao, B. Deng, F. Li, M. Huang, Y. Sun, J. Li and F. Dong, *J. Hazard. Mater.*, 2021, **420**, 126577.